APPLIED SCIENCES AND ENGINEERING

Multilayer fabrication of durable catheter-deployable soft robotic sensor arrays for efficient left atrial mapping

Varun Kashyap, Alexandre Caprio, Tejas Doshi, Sun-Joo Jang, Christopher F. Liu*, Bobak Mosadegh†, Simon Dunham†

Devices that perform cardiac mapping and ablation to treat atrial fibrillation provide an effective means of treatment. Current devices, however, have limitations that either require tedious point-by-point mapping of a cardiac chamber or have limited ability to conform to the complex anatomy of a patient's cardiac chamber. In this work, a detailed, scalable, and manufacturable technique is reported for fabrication of a multielectrode, soft robotic sensor array. These devices exhibit high conformability (~85 to 90%) and are equipped with an array of stretchable electronic sensors for voltage mapping. The form factor of the device is intended to match that of the entire left atrium and has a hydraulically actuated soft robotic structure whose profile facilitates deployment from a 13.5-Fr catheter. We anticipate that the methods described in this paper will serve a new generation of conformable medical devices that leverage the unique characteristics of stretchable electronics and soft robotics.

INTRODUCTION

Atrial fibrillation (AFib) is the most common form of cardiac arrhythmia, with a worldwide prevalence of more than 33 million people worldwide (*1*). AFib causes an irregular and often rapid heart rate that may cause symptoms like palpitations, fatigue, and shortness of breath. It originates from the interplay between genetic predisposition, ectopic electrical activity, and abnormal atrial tissue substrate (*2*). AFib can affect the efficiency of cardiac output and promote the formation of blood clots inside the left atrium (particularly the left atrial appendage). If these clots embolize and travel from the heart to the brain, they could result in a stroke; AFib is associated with a 1.5- to 2-fold increase in death and heart failure and about 3- to 5-fold higher risk of stroke (*3*, *4*). Furthermore, AFib is also associated with a greater risk of hospitalization, with 10 to 40% of patients with this disease hospitalized annually (*5*).

Radiofrequency catheter ablation has emerged as an established and widespread technique for the treatment of AFib via a minimally invasive catheter procedure. Cardiac electrograms are mapped using a sensing catheter, and then radiofrequency energy is applied to the heart muscle at particular locations to cauterize the circuits that trigger AFib, using an ablation catheter. This procedure has been shown to be superior to antiarrhythmic drug therapy in providing rhythm control in patients with paroxysmal and persistent AFib (*6*). There is strong evidence that AFib ablation therapy improves quality of life, reduces health resource utilization, and improves heart function in patients with heart failure (*7*–*9*). For the ablation procedure, electroanatomical mapping techniques have been developed to guide the procedure. By recording the electrical activity inside the heart, the circuits that are generating AFib can be identified. However, current electroanatomical mapping systems have limited spatiotemporal resolution for detecting localized AFib drivers because of their sequential spatiotemporal characteristics, intermittent firing, and complex atrial anatomy (*10*). These are some of the reasons for suboptimal outcomes after ablation in some forms of AFib (*11*). Subsequently, advanced mapping catheters such as basket catheters with multielectrode arrays were introduced to mitigate this drawback (*12*–*15*). The advantages of multielectrode mapping include quicker voltage mapping and more accurate assessment of activation sequence. However, conventional multielectrode catheter designs are fabricated from sensor arrays that are deployed on a cage of inelastic materials (either metal wire or narrow strips of inelastic polymer film) designed to passively engage with tissue. These designs have limited conformability and other nonideal mechanical response, such as spline bunching (i.e., a nonuniform distribution of the sensor arrays due to improper deployment/expansion of the device in the left atrium). The effective result of these unintended mechanical responses is that less than 50% of the sensors provide meaningful data (*16*–*18*). Here, we report the development of a soft robotic sensor array (SRSA) that uniformly conforms 128 flexible sensors to the left atrial tissue by hydraulically actuating a thin-walled polymer cage. We deployed these devices in four soft three-dimensional (3D) printed atrial models and found that an average of ~85 to 90% of the sensors expected to make tissue contact establish robust near-field sensing [<2 mm distance, as assessed by micro–computed tomography (μ-CT) (*19*)]. Details regarding the number of sensors in contact are explained further in the Supplementary Materials (table S1). Further, we were able to show the robustness of our designs by deploying them from a 13.5-Fr catheter tube (fig. S3) and showing that sensors could undergo 100 cycles of actuation without reduction of performance.

Overall, development of these devices posed several challenges, namely, scalable fabrication, integration, and associated mechanical durability. To achieve conformable SRSAs, we used unique approaches for fabricating soft actuator designs with high degrees of complexity (*20*). We focused on designs that have been established for their ability to conform to patient atria (*21*). Here, we have developed an approach for postprocessing flex-PCB (printed circuit board) with serpentine sensor array designs and integrating them with these approaches for soft actuator fabrication that can yield complex geometry SRSAs with

Dalio Institute for Cardiovascular Imaging, Department of Radiology, Weill Cornell Medicine, New York, NY 10021, USA.
*Present address: Department of Cardiology, Weill Cornell Medicine, New York, NY 10021, USA.
†Corresponding author. Email: sid2012@med.cornell.edu (S.D.); bom2008@med.cornell.edu (B.M.)

128 sensors. We describe a self-aligned postprocessing method to remove inelastic flex-PCB substrates, providing them markedly increased flexibility, required for integration with soft actuators. These novel methods allow these devices to be fabricated without costly and time-consuming cleanroom fabrication, using scalable flex-PCB manufacturing. We believe that the principles, procedures, and techniques discussed in this study can be valuable tools not only for this application but also for a wide variety of applications, where sensor arrays are integrated with soft actuators, especially when thin or low-profile designs are needed.

RESULTS AND DISCUSSION

Starting from factory-manufactured flex-PCB sensor array and thermoplastic polyurethane (TPU) sheets, a final cage device (i.e., SRSAs) is manufactured, which has high conformability in the left atrium. Figure 1 illustrates the key features of the SRSA design and its application for atrial mapping. Note that both transparent and colored TPU films can be used to fabricate these SRSAs (see Materials and Methods in the Supplementary Materials for more details). A laser-cutting postprocessing step is introduced in this study to convert the flex-PCB sensor arrays to stretchable sensor arrays as discussed in a later part of this study. Soft robotic actuators are fabricated from the TPU sheets using a combination of laser-cutting and heat-pressing steps. The stretchable sensor arrays are integrated with the soft robotic actuators to fabricate a single linear SRSA. Using a method for fabricating actuators with complex 2D geometry based on laser cutting (*20*, *22*), a complete fabricated SRSA cage was made with eight coupled linear actuators, each with 16 sensors. In the figure, SRSAs fabricated from transparent TPU allow for better visualization of the integrated flexible sensor arrays. Individual serpentine traces are visible in the inset. For typical atrial mapping procedures, an electrophysiologist would deploy the SRSA cage from a catheter through the puncture made in the foramen ovale in the patient's septal wall, which is the heart tissue that separates the right and left atrium. Here, devices were deployed in soft 3D printed atria based on real patient CT images to assess the conformability of the device. Soft tissue–like materials (TangoPlus) were used in the 3D printed models to mimic the mechanical properties of the atrial tissue (*23*–*26*). This is explained further in Materials and Methods.

The SRSAs were fabricated using a method that allows for creation of actuators with arbitrary 2D complexity, based on laser cutting and subsequent heat-pressed assembly of TPU and sacrificial poly vinyl alcohol (PVA) films, described elsewhere (*20*, *22*, *27*, *28*). We coupled this with 3D assembly of various 2D actuator patterns to yield the 3D soft actuator cage used in our design. The specific design and assembly used to fabricate our SRSAs designs are shown in the Supplementary Materials, figs. S1 and S2. In short, 2D actuators are formed by laser-cutting 2D patterns of water-soluble PVA and using it as a sacrificial layer to form closed channels between two bonded layers of TPU. While this process allows actuator geometries with notable complexity, it has the benefit that because it consists of an assembly of 2D planar actuator designs, these designs are intrinsically compatible with most scalable manufacturing methods for electronics. This is in contrast to many alternative methods to fabricate soft robotic actuators that require complex embedded 3D channels to allow for integration of sensors or electronics (*29*). In addition, most other actuators are intrinsically high strain (~100 to 400%) to yield actuation, and thus, they rely on materials with greater intrinsic stretchability than conventional flex-PCBs (*30*, *31*). These limit the scalability of such designs.

Postprocessing of stretchable electronics

To provide electronics with the flexibility required for the integration with our soft actuators, we developed a versatile laser-cutting postprocessing method to convert inelastic flex-PCB substrates into stretchable sensors. This technique presents several notable benefits: (i) Fabrication of stretchable sensor arrays can be done using flex-PCB as a scalable starting component. (ii) The process is self-aligned, thus preserving the substrate polyimide (PI) material only under the individual traces, thus allowing for greater durability and robustness than isolated metal traces alone. (iii) Unlike alternative methods that remove the substrate entirely (e.g., etching), this technique can arbitrarily pattern stretchable regions, while other regions can remain stiff. (iv) The resolution of laser postprocessing can be in the order of 10 μm. (v) The use of electronic sensor arrays without laser postprocessing results in significant reduction in conformability, which can be seen in fig. S12.

Here, the flexible electronics were manufactured initially in a flex house (PCB Universe). The design consists of three layers (Fig. 2A), namely, a copper layer sandwiched between two PI layers. The copper layer consists of serpentine traces connected to 16 electrodes on each flexible circuit board. Windows are provided on the top PI layer to expose the electrodes for contact. The detailed schematic of the initial flex-PCB design is shown in the Supplementary Materials and fig. S5. The thickness of the PI layer is ~20 μm and that of the copper layer is 15 μm, as measured from the scanning electron microscope (SEM) image shown in fig. S4. Therefore, the flex-PCB initially has a uniform thickness between ~40 and ~50 μm. The extent to which the flex-PCB can be actuated in the inflatable frame is a direct function of its thickness. Therefore, to ensure better actuation and subsequently better conformability of these electronics within the left atrium, a postprocessing step was incorporated within the workflow. A CO_2 laser (Universal Laser, power 23%, speed 50%) was used to selectively remove the PI from sections of the flex-PCB as shown in Fig. 2B. The laser rasters as indicated by dashed lines in the figure, thereby removing the excess PI. Note that laser conditions were optimized such that the PI is preserved underneath the traces. We believe that this is likely due to thermal masking, whereby the copper traces allow for heat to be rapidly spread, reducing peak temperatures and preventing the underlying PI from reaching temperatures sufficient for removal. Meanwhile, regions of PI not in contact with thermally conductive copper reached higher peak temperatures and were subsequently removed. We enhanced the stability of the entire array and prevented traces from losing alignment to one another by preserving the PI substrate as thin strips that connect neighboring traces (Fig. 2C). In addition, the insulation in the topcoat PI could be used for electrical isolation in regions where it is preserved. Cross-sectional (end-on) confocal images of the flex-PCB were taken before and after the laser-cutting process. The copper layer (black) can be seen sandwiched between two PI layers (fluorescent green) in Fig. 2D. However, only one layer of bottom PI can be seen after the laser-cutting process in Fig. 2E. Figure 2F shows the SEM image of the flex-PCB after the postprocessing. To test the stretchability of an SRSA, a tensile test was conducted on a flex-PCB and a postprocessed array, both of which were sandwiched between two thermally bonded layers of TPU (Fig. 2G). A marked increase in strain can be observed from ~0.9% before postprocessing to ~30% after postprocessing

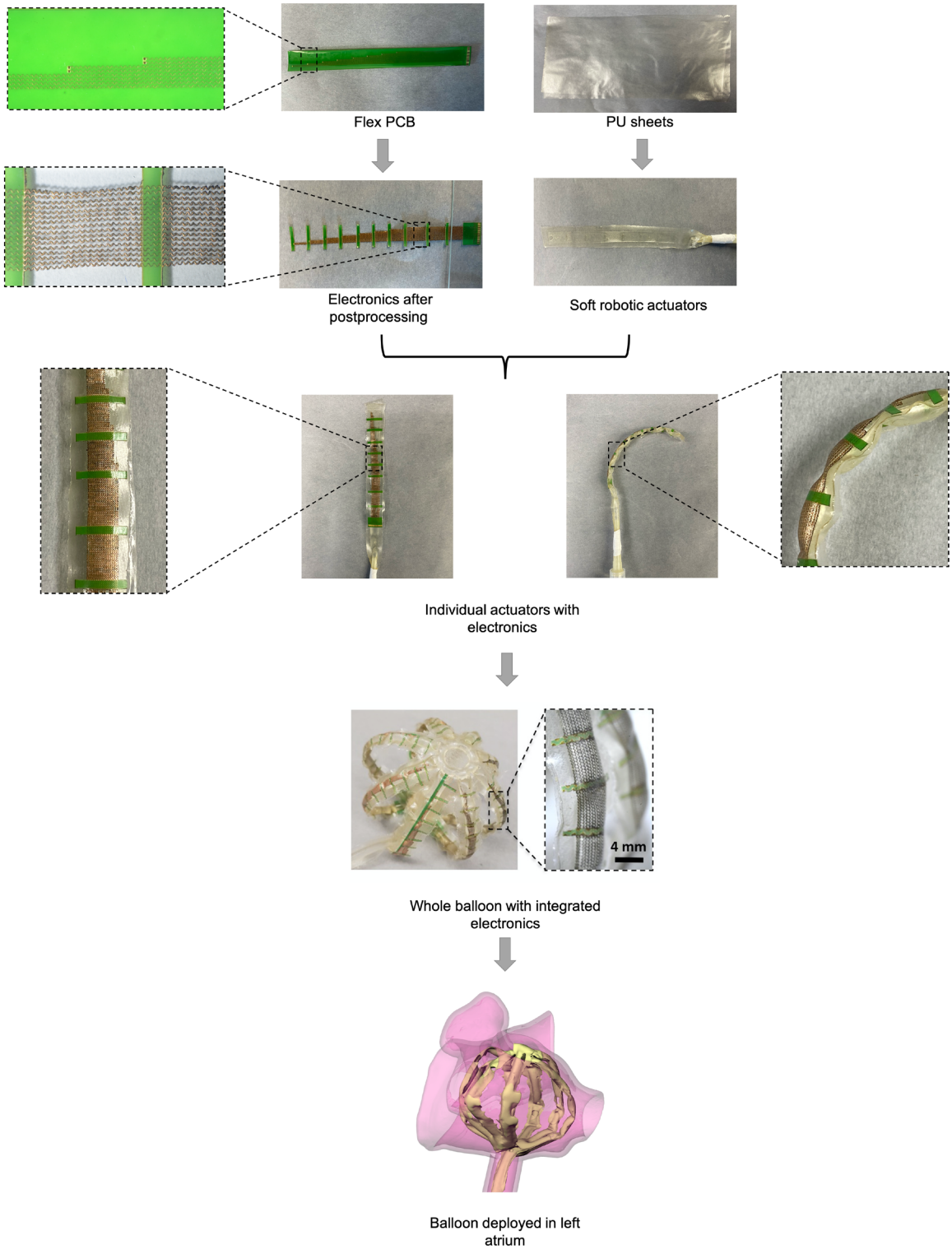

Fig. 1. Overview of the biosensor integrated catheter-deployable balloon. Flex-PCB and TPU sheets are processed through various fabrication techniques to obtain a single linear SRSA from which an SRSA cage device is fabricated. This device is inserted into the left atrium using a mock catheter through the puncture made in the foramen ovale in the patient's septal wall. Photo credit: Varun Kashyap and Alexandre Caprio, Weill Cornell Medicine.

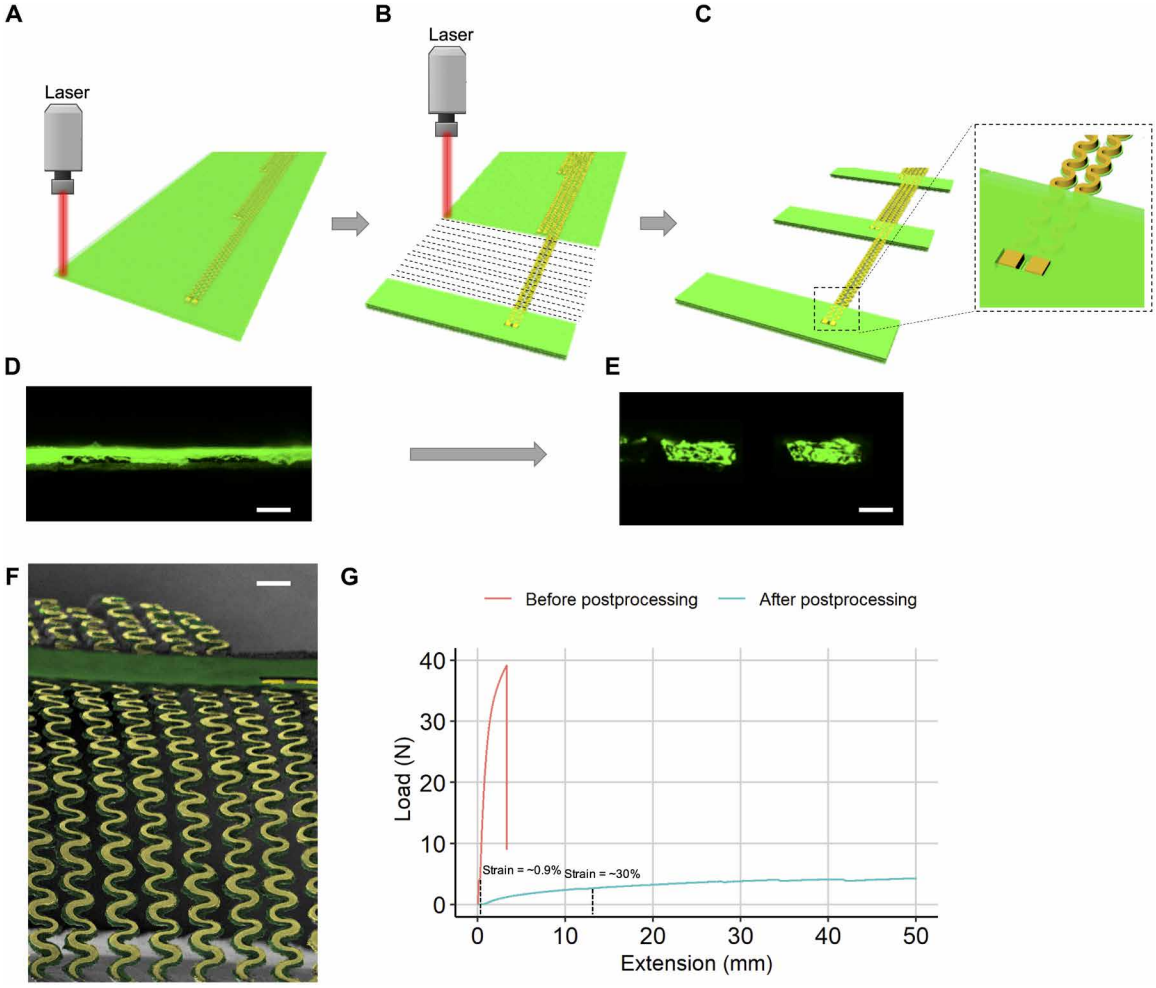

Fig. 2. Postprocessing of stretchable electronics. (**A**) Stretchable electronics before laser cutting. (**B**) The selective laser-cutting process. The rastering path of the laser is depicted. (**C**) Stretchable electronics after postprocessing. Inset shows the underlying PI preserved after the laser-cutting process. (**D**) Cross-sectional (end-on) confocal image of the electronics before laser cutting. Scale bar, 0.1 mm. (**E**) Cross-sectional (end-on) confocal image of the electronics after laser cutting. Scale bar, 0.1 mm. (**F**) SEM image of the final laser-cut stretchable electronics. Scale bar, 0.3 mm. (**G**) Results for the tensile test are shown between preprocessed and postprocessed sensor arrays. The stretchability of the postprocessed sensor arrays can be clearly observed.

at the breaking point of the serpentines, thereby showing excellent stretchability of the SRSAs. Details of this experiment are explained further in the Supplementary Materials (fig. S6). Note that preprocessed flex-PCB alone is incompatible with the soft actuators used for this design, as it is too stiff and inelastic to allow for actuation. Therefore, this postprocessing step is critical for the success of the overall fabrication method.

Durability analysis of stretchable electronics integrated soft actuators

Two separate experiments were conducted to evaluate the durability of the SRSAs. These results are shown in Fig. 3. In one experiment, one leg of the SRSA cage was actuated multiple times, and the resulting conductivity of the individual sensor traces was subsequently assessed (Signatone probe station, Tektronix 4200 parameter analyzer), as shown in Fig. 3A. The actuation was carried out by applying a pressure of 10 psi (68.95 kPa), which yielded a level of overall actuation consistent with those observed in the device (Fig. 1A) and repeated for 100 iterations to evaluate the long-term durability of the electronics under repeated loading and deformation. For each of the electrodes, the current-voltage relation (*I-V*) sweep was recorded, and the resistance values were plotted as shown in Fig. 3. The values remain within the SD even after 100 iterations, showing excellent durability of the stretchable electronics. Resistance values for each trial are tabulated in the Supplementary Materials. μ-CT images and volume-rendered segmentations of individual linear SRSA are shown in Fig. 3B; the inset shows the SRSA. One reason these designs are able to demonstrate this type of durability is the low strain actuator design used (*20*). To understand the local strain observed in the sensor arrays themselves, strain in the copper traces along the length of the stretchable electronics was evaluated experimentally using confocal imaging, and finite element analysis (FEA) simulations (ANSYS workbench 19) were performed to validate these results. Note that maximum deformation occurs in the pockets that are along the length of the actuator legs. The pockets are part of the linear actuator design applied here, which allow for low strain actuation (*20*). They are formed by patterning the sacrificial PVA layer in a manner to allow the TPU to fuse in regions of the actuators, such that it subsequently inflates in discrete

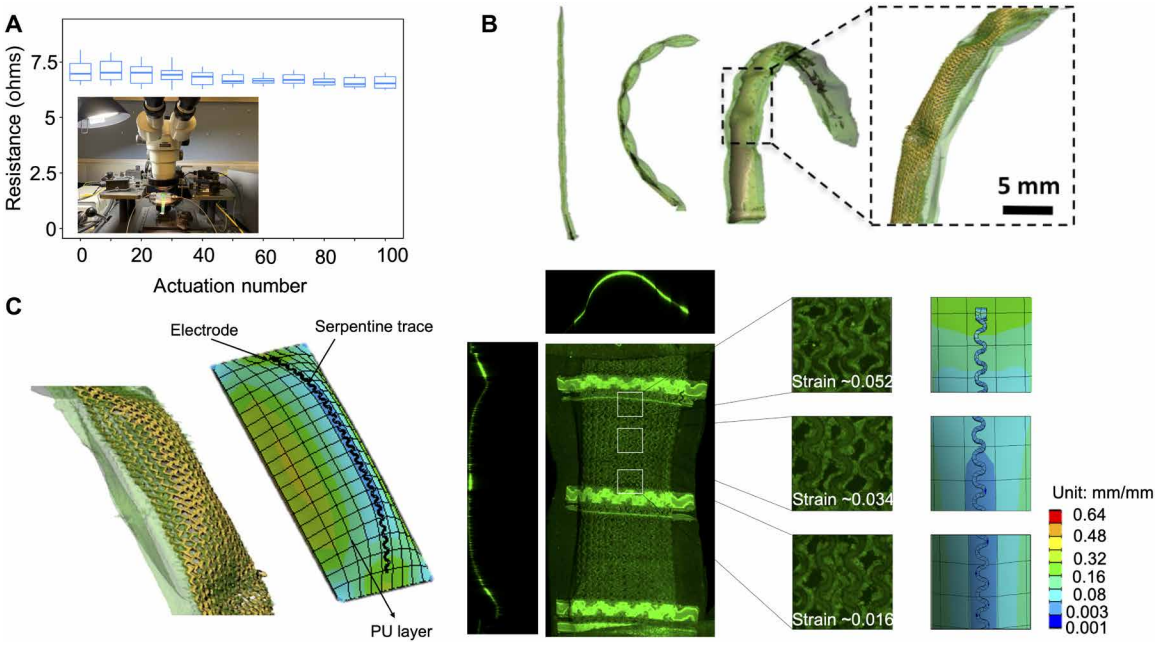

Fig. 3. Mechanical stability and durability analysis. (**A**) Plot shows resistance as a function of actuations for a single actuator. The actuation was carried out at 10 psi (68.95 kPa). Inset shows the probe station used to measure resistance using an *I-V* sweep. (**B**) μ-CT images and volume-rendered segmentations of actuated linear SRSA are shown. (**C**) Actuation pocket where maximum deformation takes place is simulated using ANSYS workbench. Strain values are compared between confocal images for an actuated pocket and that obtained from FEA analysis. Photo credit: Varun Kashyap, Weill Cornell Medicine.

pockets. This can be clearly observed in Fig. 3B. This pocket section is considered to measure maximum strain in both experiments and simulations. To evaluate the strain experimentally, confocal images of the SRSA in both its nonactuated and actuated states were recorded. The average strain in each section of the traces was calculated using the deformation values between the two states. FEA analysis was conducted using the static structural module of ANSYS workbench. A hyperplastic model was defined as discussed in an earlier paper (*20*), and the balloon was actuated by applying a uniform pressure loading of 10 psi (68.95 kPa). Details of the simulation are explained further in the Supplementary Materials. Comparison between experimental and simulated results is shown in Fig. 4C. The figure shows negligible strain along the length of the traces in the actuated state. The strain is maximum at the ends of the pocket region. We believe that this is due to the constraint that is provided based on the design of these actuators. However, this maximum strain is well within the design limits for copper (*32*), thereby allowing these stretchable electronics to go through many actuation cycles. The alignment between experimental observation and simulation provides insight into the robustness and durability of these designs.

In vitro voltage mapping evaluations were performed on a single array of sensors (16 sensors, associated with a single actuator leg) using a cardiac tissue phantom. Figure S8 shows the ability of SRSA to resolve the signal in a range of pulse widths and voltages encompassing values typical for cardiac electrograms to the tissue phantom. Figure S9 shows the representative sensor data from SRSA for low voltage (2 mV) and low pulse width (50 ms) in phosphate-buffered saline for near-field sensing (between 0.5 and 2 mm). To characterize sensors on multiple splines, measured signal pulse width averaged over 64 sensors is plotted and compared with control signals in fig. S20. This demonstrates the sensors' ability to read electrograms effectively.

μ-CT conformability experiments

The overall goal of creating SRSAs with active soft actuators is to provide designs for sensor arrays that have the ability to conform to complex patient anatomies. Several commercial spline-based catheters are being developed for improved treatment of AFib with better conformability. Among these, two representative examples, Constellation (Boston Scientific, MA) and FIRMap (Abbott, IL), are discussed (*33*). Constellation (Boston Scientific, MA) catheter, which is more widely used, has several drawbacks including interspline bunching resulting in loss of coverage and contact and the lack of electrode poles proximally resulting in loss of septal coverage (*17*, *34*). To determine conformability, an earlier study (*33*) used a simplified version of the left atrium segmented model. Electrodes within 10 mm of the left atrium geometry were projected onto the geometry and marked as covering an area having a radius of 10 mm. Thus, the total atrial coverage achieved by the electrodes is calculated as a percentage of left atrium geometry surface area excluding the vascular and valvular structures. The average conformability using these catheters was ~50%. FIRMap (Abbott, IL) catheters were designed as improvements over Constellation (Boston Scientific, MA) catheters (*33*). They have stiffer splines intended to minimize distortion and bunching. Electrode spacing is also increased with more proximal electrodes aiming to improve left atrial septal coverage. However, even with these improvements, they showed an average conformability of ~76% in the left atrium (*33*). Overall, conventional catheters are limited by electrode position, poor tissue contact, and spline bunching, which leads to poor electrical coverage within the left atrium. To assess the conformability of SRSAs, they were deployed in four patient-specific 3D printed left atria and actuated at 10 psi (68.95 kPa) to obtain its final configuration within the left atrium. μ-CT images (Siemens Inveon Multimodality Scanner) and volume-rendered segmentations (Mimics 19) of deployed

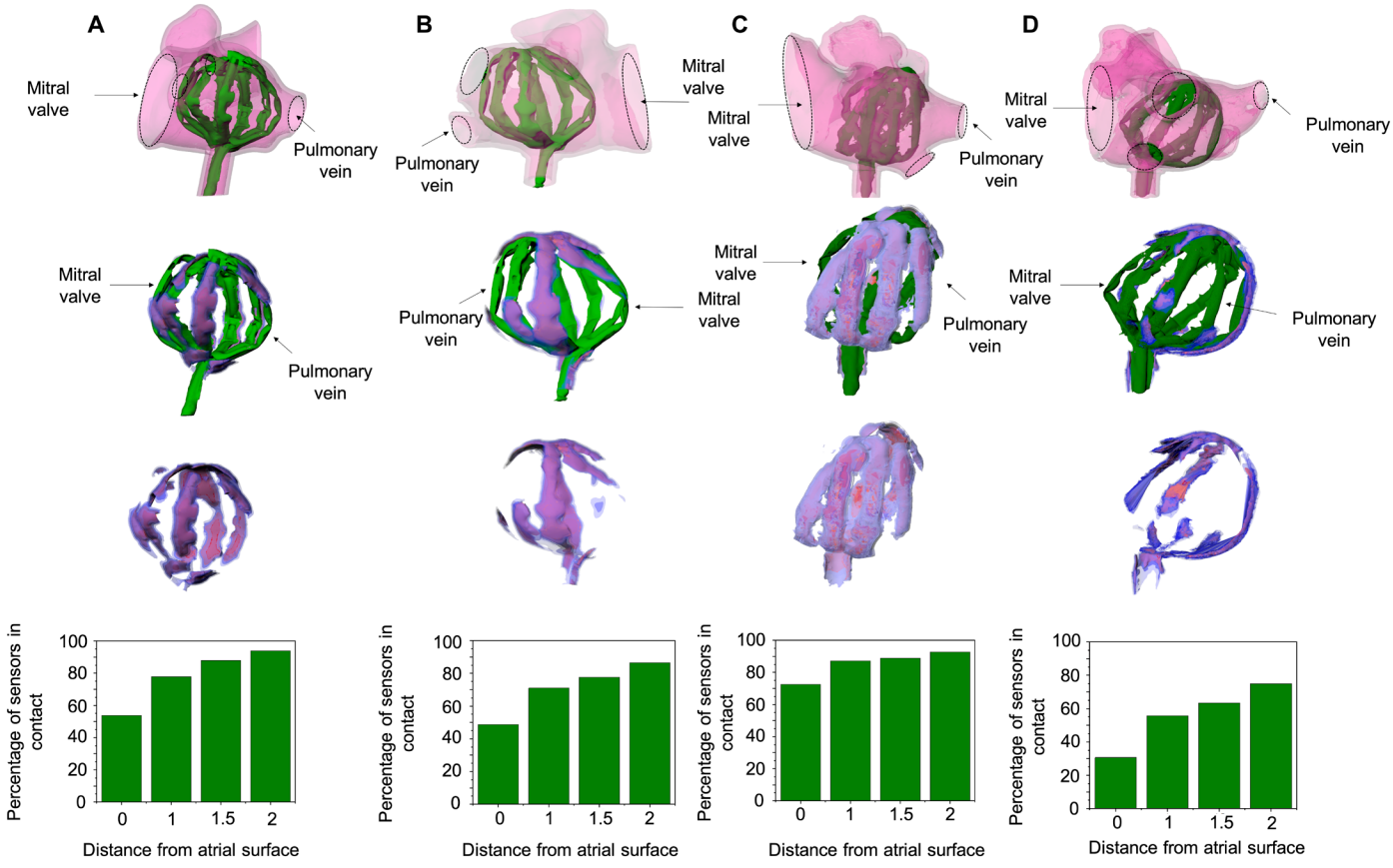

Fig. 4. Conformability analysis. SRSA is deployed in four patient-specific 3D printed left atria, and the μ-CT images and volume-rendered segmentations are shown in figures (**A**) to (**D**). The heatmaps indicate the distance of SRSA from the atrial surface. This ranges between 0 and 2 mm with the spectrum moving from red to blue. Accounting for the voids in the geometry of the left atrium (mitral valve and pulmonary vein), the percentage of number of sensors in contact is plotted as a function of distance for each of the atria. An average conformability of ~85 to 90% was observed.

SRSAs were used to analyze its conformability. The results are shown in Fig. 4. The first row shows the SRSA cage deployed into the 3D printed atria via a mock catheter through the puncture made in the foramen ovale in the patient's septal wall. The SRSA cage conforms to the atrial surface effectively and shows no spline bunching (i.e., the individual linear actuators that form the SRSA cage were evenly distributed within the atria). Using mesh Boolean operations, the regions of intersections were obtained for each of these atria. Prior studies have shown that the signals can be detected by the sensors at distances greater than 2 mm from the atrial surface (*19*, *35*). Considering these values, we color-coded different distances from 0 to 2 mm analogous to a thermal heatmap with the spectrum ranging from red to blue. These heatmaps are superimposed on the SRSAs to show regions that are in direct contact with the atrial tissue. Graphs depicting the proportion of sensors within a given distance from the atrial surface are plotted for each atrium. For these calculations, sensors that were not near tissue because they were adjacent to anatomic features such as the pulmonary veins or the left atrial appendage were ignored. SRSAs show an average conformability of ~85 to 90% for these randomly chosen patient-specific 3D printed patient atria. Atrium 4 shows the least conformability of 75%. We believe that this is associated with the buckling of the SRSAs that can be clearly observed from the figure. Designs that mitigate this type of buckling or creating cages with appropriate sizing may represent a strategy to further increase the conformability of these devices. To address the dynamic motion of the device, we deployed it in the left atria of an excised porcine cadaver (unfixed tissue) and used a pulsatile flow loop (Shelley Medical) to produce realistic flow and deformations as shown in fig. S10. SRSA shows excellent conformability under dynamic flow conditions as shown in fig. S11. The videos associated with these experiments are provided as movies S1 and S2, and a detailed description is provided in the Supplementary Materials.

Conclusion

In this study, we report the development of SRSAs exhibiting excellent mechanical durability and conformability when deployed within patient-specific 3D printed left atria. This method used to create these SRSAs illustrates a promising strategy for integration of soft robotics and flexible electronics for medical applications, especially those deployed via a minimally invasive catheter. We demonstrated the mechanical durability of these devices by showing that sensors could undergo 100 cycles of actuation without reduction of performance. Furthermore, simulations were performed to assess the strain in electronics, which showed good match with the experimental values. We deployed SRSAs using a 13.5-Fr mock catheter into patient-specific soft 3D printed left atria (soft materials mimicking the atrial tissue) to analyze its conformability. SRSA shows an average conformability

of ~85 to 90% within these atria. We also developed a novel method for scalable fabrication and integration of flexible electronics that provides a versatile approach for creating a wide variety of complex geometry actuator/sensor arrays that are broadly applicable. This enables future development of efficient devices for better treatment of AFib and cardiac arrhythmias. Future work should focus on reducing the profile of the device to be more consistent with other clinical electrophysiology devices (~8 Fr) and assessing conformability under more realistic conditions (beating heart models with pulsatile flow) or in large animal models.

MATERIALS AND METHODS

The stack up of all the layers is shown in fig. S1. Note that this procedure is critical for the integration of electronics into these devices. Each step along with the dimensions of individual components is designed considering the integration of stretchable electronics. To fabricate the SRSAs, we first laser cut sheets of PVA into their desired 2D geometry and sandwich it between two layers of TPU. PVA is used mainly for two purposes: (i) to prevent the bonding of the TPU layers and (ii) to act as a sacrificial layer and facilitate a path for the flow of the liquid (viz. water) during hydraulic actuation. The overall thickness of the inflatable frame can be varied based on the number of layers of TPU used. Before integrating the flex-PCB sensor arrays with the soft robotic actuators, a postprocessing was carried out on the stretchable electronics with a unique laser-cutting step, as described in described under the section 'Postprocessing of stretchable electronics'. An additional layer of TPU is heat-pressed on top of the stretchable sensor array to encapsulate them. Windows are laser cut to expose the sensor pads themselves.

For balloons deployed in patient atria, a somewhat more complex fabrication approach was used to ensure that the hydraulic input was in line with the device itself, allowing it to be deployed via a catheter as shown in fig. S2. The inflatable frame is fabricated in two parts, the hub and the legs. In this step, the TPU and PVA sheets are laser cut to the desired configuration. In step 3, before integrating the electronics with the laser-cut legs, a postprocessing was carried out on the stretchable electronics with a unique laser-cutting step. Stretchable electronics, after postprocessing, are aligned with PU sheets with laser-cut windows that expose the electrodes when in contact with the left atrial tissue. This also serves as the topmost layer of the final stack up. In the next step (step 4), the precut legs are integrated with windows and electronics using a heat press (138°C for 600 s). Subsequently, laser-cut TPU and PVA forming the hub are also heat-pressed under the same conditions. In step 5, as shown in fig. S2, the heat-pressed hub and legs are integrated together to form the final balloon. Adaptors crafted out of PVA are used in this process to prevent leaks and ensure contact between these parts. Once the complete SRSAs are fabricated, the sacrificial PVA layer is removed by perfusing the actuators with water.

SUPPLEMENTARY MATERIALS

Supplementary material for this article is available at http://advances.sciencemag.org/cgi/content/full/6/46/eabc6800/DC1

REFERENCES AND NOTES

1. S. S. Chugh, R. Havmoeller, K. Narayanan, D. Singh, M. Rienstra, E. J. Benjamin, R. F. Gillum, Y. H. Kim, J. H. McAnulty, Z. J. Zheng, M. H. Forouzanfar, M. Naghavi, G. A. Mensah, M. Ezzati, C. J. L. Murray, Worldwide epidemiology of atrial fibrillation: A global burden of disease 2010 study. *Circulation* **129**, 837–847 (2014).
2. J. Heijman, N. Voigt, S. Nattel, D. Dobrev, Cellular and molecular electrophysiology of atrial fibrillation initiation, maintenance, and progression. *Circ. Res.* **114**, 1483–1499 (2014).
3. P. A. Wolf, T. R. Dawber, H. E. Thomas, W. B. Kannel, Epidemiologic assessment of chronic atrial fibrillation and risk of stroke: The framingham study. *Neurology* **28**, 973–977 (1978).
4. H. Calkins, G. Hindricks, R. Cappato, Y. H. Kim, E. B. Saad, L. Aguinaga, J. G. Akar, V. Badhwar, J. Brugada, J. Camm, P. S. Chen, S. A. Chen, M. K. Chung, J. C. Nielsen, A. B. Curtis, D. W. Davies, J. D. Day, A. d'Avila, N. M. S. de Groot, L. Di Biase, M. Duytschaever, J. R. Edgerton, K. A. Ellenbogen, P. T. Ellinor, S. Ernst, G. Fenelon, E. P. Gerstenfeld, D. E. Haines, M. Haissaguerre, R. H. Helm, E. Hylek, W. M. Jackman, J. Jalife, J. M. Kalman, J. Kautzner, H. Kottkamp, K. H. Kuck, K. Kumagai, R. Lee, T. Lewalter, B. D. Lindsay, L. Macle, M. Mansour, F. E. Marchlinski, G. F. Michaud, H. Nakagawa, A. Natale, S. Nattel, K. Okumura, D. Packer, E. Pokushalov, M. R. Reynolds, P. Sanders, M. Scanavacca, R. Schilling, C. Tondo, H. M. Tsao, A. Verma, D. J. Wilber, T. Yamane, 2017 HRS/EHRA/ECAS/APHRS/SOLAECE expert consensus statement on catheter and surgical ablation of atrial fibrillation. *J. Arrhythmia* 10.1016/j.joa.2017.07.001, (2017).
5. B. A. Steinberg, S. Kim, G. C. Fonarow, L. Thomas, J. Ansell, P. R. Kowey, K. W. Mahaffey, B. J. Gersh, E. Hylek, G. Naccarelli, A. S. Go, J. Reiffel, P. Chang, E. D. Peterson, J. P. Piccini, Drivers of hospitalization for patients with atrial fibrillation: Results from the Outcomes Registry for Better Informed Treatment of Atrial Fibrillation (ORBIT-AF). *Am. Heart J.* **167**, 735–742.e2 (2014).
6. H. Calkins, M. R. Reynolds, P. Spector, M. Sondhi, Y. Xu, A. Martin, C. J. Williams, I. Sledge, Treatment of atrial fibrillation with antiarrhythmic drugs or radiofrequency ablation: Two systematic literature reviews and meta-analyses. *Circ. Arrhythmia Electrophysiol.* **2**, 349–361 (2009).
7. C. Blomström-Lundqvist, S. Gizurarson, J. Schwieler, S. M. Jensen, L. Bergfeldt, G. Kennebäck, A. Rubulis, H. Malmborg, P. Raatikainen, S. Lönnerholm, N. Höglund, D. Mörtsell, Effect of catheter ablation vs antiarrhythmic medication on quality of life in patients with atrial fibrillation: The CAPTAF randomized clinical trial. *JAMA* **321**, 1059–1068 (2019).
8. M. Samuel, M. Avgil Tsadok, J. Joza, H. Behlouli, A. Verma, V. Essebag, L. Pilote, Catheter ablation for the treatment of atrial fibrillation is associated with a reduction in health care resource utilization. *J. Cardiovasc. Electrophysiol.* **28**, 733–741 (2017).
9. R. J. Hunter, T. J. Berriman, I. Diab, R. Kamdar, L. Richmond, V. Baker, F. Goromonzi, V. Sawhney, E. Duncan, S. P. Page, W. Ullah, B. Unsworth, J. Mayet, M. Dhinoja, M. J. Earley, S. Sporton, R. J. Schilling, A randomized controlled trial of catheter ablation versus medical treatment of atrial fibrillation in heart failure (the CAMTAF trial). *Circ. Arrhythmia Electrophysiol.* **7**, 31–38 (2014).
10. T. Rostock, M. Rotter, P. Sanders, Y. Takahashi, P. Jaïs, M. Hocini, L. F. Hsu, F. Sacher, J. Clémenty, M. Haïssaguerre, High-density activation mapping of fractionated electrograms in the atria of patients with paroxysmal atrial fibrillation. *Heart Rhythm* **3**, 27–34 (2006).
11. A. Verma, C. Y. Jiang, T. R. Betts, J. Chen, I. Deisenhofer, R. Mantovan, L. Macle, C. A. Morillo, W. Haverkamp, R. Weerasooriya, J. P. Albenque, S. Nardi, E. Menardi, P. Novak, P. Sanders; STAR AF II Investigators, Approaches to catheter ablation for persistent atrial fibrillation. *N. Engl. J. Med.* **372**, 1812–1822 (2015).
12. B. Berte, J. Relan, F. Sacher, X. Pillois, A. Appetiti, S. Yamashita, S. Mahida, F. Casassus, D. Hooks, J. M. Sellal, S. Amraoui, A. Denis, N. Derval, H. Cochet, M. Hocini, M. Haïssaguerre, R. Weerasooriya, P. Jaïs, Impact of electrode type on mapping of scar-related VT. *J. Cardiovasc. Electrophysiol.* **26**, 1213–1223 (2015).
13. S. L. Chang, Y. J. Lin, C. T. Tai, L. W. Lo, T. C. Tuan, A. R. Udyavar, Y. F. Hu, S. J. Chiang, W. Wongcharoen, H. M. Tsao, K. C. Ueng, S. Higa, P. C. Lee, S. A. Chen, Induced atrial tachycardia after circumferential pulmonary vein isolation of paroxysmal atrial fibrillation: Electrophysiological characteristics and impact of catheter ablation on the follow-up results. *J. Cardiovasc. Electrophysiol.* **20**, 388–394 (2009).
14. D. A. Hooks, S. Yamashita, S. Capellino, H. Cochet, P. Jais, F. Sacher, Ultra-rapid epicardial activation mapping during ventricular tachycardia using continuous sampling from a high-density basket (OrionTM) catheter. *J. Cardiovasc. Electrophysiol.* **26**, 1153–1154 (2015).
15. E. Anter, C. M. Tschabrunn, F. M. Contreras-Valdes, J. Li, M. E. Josephson, Pulmonary vein isolation using the Rhythmia mapping system: Verification of intracardiac signals using the Orion mini-basket catheter. *Heart Rhythm* **12**, 1927–1934 (2015).
16. C. Schmitt, B. Zrenner, M. Schneider, M. Karch, G. Ndrepepa, I. Deisenhofer, S. Weyerbrock, J. Schreieck, A. Schömig, Clinical experience with a novel multielectrode basket catheter in right atrial tachycardias. *Circulation* **99**, 2414–2422 (1999).
17. J. Laughner, S. Shome, N. Child, A. Shuros, P. Neuzil, J. Gill, M. Wright, Practical considerations of mapping persistent atrial fibrillation with whole-chamber basket catheters. *JACC Clin. Electrophysiol.* **2**, 55–65 (2016).
18. T. Oesterlein, D. Frisch, A. Loewe, G. Seemann, C. Schmitt, O. Dössel, A. Luik, Basket-type catheters: Diagnostic pitfalls caused by deformation and limited coverage. *Biomed. Res. Int.* **2016**, 5340574 (2016).

19. A. S. Jadidi, E. Duncan, S. Miyazaki, N. Lellouche, A. J. Shah, A. Forclaz, I. Nault, M. Wright, L. Rivard, X. Liu, D. Scherr, S. B. Wilton, F. Sacher, N. Derval, S. Knecht, S. J. Kim, M. Hocini, S. Narayan, M. Haïssaguerre, P. Jaïs, Functional nature of electrogram fractionation demonstrated by left atrial high-density mapping. *Circ. Arrhythmia Electrophysiol.* **5**, 32–42 (2012).
20. A. A. Amiri Moghadam, S. Alaie, S. Deb Nath, M. Aghasizade Shaarbaf, J. K. Min, S. Dunham, B. Mosadegh, Laser cutting as a rapid method for fabricating thin soft pneumatic actuators and robots. *Soft Robot.* **5**, 443–451 (2018).
21. N. Farokhnia, A. Caprio, V. Kashyap, S. Al'Aref, L. Baskaran, B. Mosadegh, S. Dunham, A catheter-deployable soft robotic inflatable basket for enhanced conformability to the left atrium of the heart. *Adv. Healthc. Mater.* **9**, 1900951 (2020).
22. A. A. Amiri Moghadam, A. Caprio, S. Alaie, J. K. Min, S. Dunham, B. Mosadegh, Rapid manufacturing of thin soft pneumatic actuators and robots. *J. Vis. Exp.*, 10.3791/60595 (2019).
23. A. J. Cloonan, D. Shahmirzadi, R. X. Li, B. J. Doyle, E. E. Konofagou, T. M. McGloughlin, 3D-printed tissue-mimicking phantoms for medical imaging and computational validation applications. *3D Print. Addit. Manuf.* **1**, 14–23 (2014).
24. C. N. Ionita, M. Mokin, N. Varble, D. R. Bednarek, J. Xiang, K. V. Snyder, A. H. Siddiqui, E. I. Levy, H. Meng, S. Rudin, R. C. Molthen, J. B. Weaver, Eds. (2014); http://proceedings.spiedigitallibrary.org/proceeding.aspx?doi=10.1117/12.2042266, p. 90380M.
25. C. Martin, T. Pham, W. Sun, Significant differences in the material properties between aged human and porcine aortic tissues. *Eur. J. Cardiothoracic Surg.* **40**, 28–34 (2011).
26. K. Wang, Y. Zhao, Y. H. Chang, Z. Qian, C. Zhang, B. Wang, M. A. Vannan, M. J. Wang, Controlling the mechanical behavior of dual-material 3D printed meta-materials for patient-specific tissue-mimicking phantoms. *Mater. Des.* **90**, 704–712 (2016).
27. A. A. Amiri Moghadam, S. J. Jang, A. Caprio, J. Liu, H. S. Singh, J. K. Min, S. Dunham, B. Mosadegh, Using soft robotic technology to fabricate a proof-of-concept Transcatheter Tricuspid Valve Replacement (TTVR) device. *Adv. Mater. Technol.* **4**, 1800610 (2019).
28. S. Alaie, S. S. Robinson, A. A. Amiri Moghadam, J. Auge, A. Datye, H. Sidoti, T. Doshi, S. H. Gharaie, J. K. Min, B. Mosadegh, S. Dunham, Micropatterning of nonplanar surfaces on 3D devices using conformal template vacuum bagging. *Adv. Mater. Technol.* **3**, 1700353 (2018).
29. K. J. Yu, Z. Yan, M. Han, J. A. Rogers, Inorganic semiconducting materials for flexible and stretchable electronics. *npj Flex. Electron.* **1**, 4 (2017).
30. M. D. Bartlett, A. Fassler, N. Kazem, E. J. Markvicka, P. Mandal, C. Majidi, Stretchable, high-*k* dielectric elastomers through liquid-metal inclusions. *Adv. Mater.* **28**, 3726–3731 (2016).
31. C. Majidi, Soft-matter engineering for soft robotics. *Adv. Mater. Technol.* **4**, 1800477 (2019).
32. D. H. Kim, J. Xiao, J. Song, Y. Huang, J. A. Rogers, Stretchable, curvilinear electronics based on inorganic materials. *Adv. Mater.* **22**, 2108–2124 (2010).
33. S. Honarbakhsh, R. J. Schilling, R. Providência, G. Dhillon, V. Sawhney, C. A. Martin, E. Keating, M. Finlay, S. Ahsan, A. Chow, M. J. Earley, R. J. Hunter, Panoramic atrial mapping with basket catheters: A quantitative analysis to optimize practice, patient selection, and catheter choice. *J. Cardiovasc. Electrophysiol.* **28**, 1423–1432 (2017).
34. A. K. Gupta, A. Maheshwari, R. Thakur, Y. Y. Lokhandwala, Cardiac mapping: Utility or futility? *Indian Pacing Electrophysiol. J.* **2**, 20–32 (2002).
35. J. M. Stinnett-Donnelly, N. Thompson, N. Habel, V. Petrov-Kondratov, D. D. Correa De Sa, J. H. T. Bates, P. S. Spector, Effects of electrode size and spacing on the resolution of intracardiac electrograms. *Coron. Artery Dis.* **23**, 126–132 (2012).

Acknowledgments: We thank the Dalio Institute for Cardiovascular Imaging in Radiology and E. Fung for help with the μ-CT experiments. We also thank the Advanced Science Research Center NanoFabrication Facility of the Graduate Center at the City University of New York. **Funding:** This work was supported by the U.S. Army Medical Research Acquisition Activity through the PRMRP Discovery Award under award no. W81XWH-18-1-0201. Opinions, interpretations, conclusions, and recommendations are those of the authors and are not necessarily endorsed by the U.S. Army Medical Research Acquisition Activity. **Author contributions:** V.K. contributed to the design, development, and testing of SRSA. A.C. helped with the fabrication of devices. T.D. helped with laser postprocessing and sensor characterization experiments. S.-J.J. helped with confocal experiments. C.F.L. advised on the design of devices for cardiac environments and helped with manuscript preparation. V.K. wrote the manuscript, and all authors commented on the manuscript. S.D. and B.M. conceived the idea and directed the research. **Competing interests:** V.K., A.C., B.M., and S.D. are inventors on a patent related to this work ("Conformal, Non-Occluding Sensor Array for Cardiac Mapping and Ablation") filed by Cornell University (no. 62/932,192, filed: 7 November 2019). V.K., A.C., T.D., B.M., and S.D. are inventors on a patent related to this work ("Catheter Deployable Soft-Robotic Sensor Arrays and Processing of Flexible Circuits") filed by Cornell University (no. 63/015,344, filed: 24 April 2020). The authors declare that they have no other competing interests. **Data and materials availability:** All data needed to evaluate the conclusions in the paper are present in the paper and/or the Supplementary Materials. Additional data related to this paper may be requested from the authors.

Submitted 7 May 2020
Accepted 23 September 2020
Published 13 November 2020
10.1126/sciadv.abc6800

Citation: V. Kashyap, A. Caprio, T. Doshi, S.-J. Jang, C. F. Liu, B. Mosadegh, S. Dunham, Multilayer fabrication of durable catheter-deployable soft robotic sensor arrays for efficient left atrial mapping. *Sci. Adv.* **6**, eabc6800 (2020).